Applied Catalysis B: Environmental 231 (2018) 173–181

Contents lists available at ScienceDirect

Applied Catalysis B: Environmental

journal homepage: www.elsevier.com/locate/apcatb

A porous rhodium(III)-porphyrin metal-organic framework as an efficient and selective photocatalyst for CO_2 reduction

Jiewei Liu[a], Yan-Zhong Fan[a], Xin Li[a], Zhangwen Wei[a], Yao-Wei Xu[a], Li Zhang[a,*], Cheng-Yong Su[a,b,*]

[a] MOE Laboratory of Bioinorganic and Synthetic Chemistry, Lehn Institute of Functional Materials, School of Chemistry, Sun Yat-Sen University, Guangzhou 510275, China
[b] State Key Laboratory of Applied Organic Chemistry, Lanzhou University, Lanzhou 730000, China

ARTICLE INFO

Keywords:
Rhodium(III)-porphyrin
Metal-organic frameworks
Photocatalysis
CO_2
Reduction
Room-temperature phosphorescence

ABSTRACT

A rhodium(III)-porphyrin zirconium metal-organic framework (Rh-PMOF-**1**(Zr)) has been prepared from the self-assembly of a Rh-based metalloporphyrin tetracarboxylic ligand Rh(TCPP)Cl (TCPP = tetrakis(4-carboxyphenyl)porphyrin) with $ZrCl_4$. The framework of Rh-PMOF-**1** is stable up to 270 °C as disclosed by the variable-temperature powder X-ray diffraction (VT-PXRD) measurements, and possesses good chemical stability over a wide range of solvents including water. The single-crystal structural analysis reveals that Rh-PMOF-**1** contains 3-D channels (1.9 × 1.9 nm^2), and the Rh-porphyrin units are exposed to the cavities. The calculation based on the N_2 adsorption at 77 K shows Rh-PMOF-**1**(Zr) has a high BET surface area (3015 m^2g^{-1}). The luminescence decay of Rh-PMOF-**1** is well fitted to a tri-exponential curve featuring a long average lifetime of 207 μs at 298 K under vacuum, which represents a rare example of room-temperature phosphorescence of Rh-porphyrin complexes. Under 1 atm, it displays CO_2 uptake up to 42, 53 and 98 cm^3g^{-1} at 308, 298 and 273 K, respectively. Catalytic results show that, under the visible light (≥ 400 nm) irradiation without any additional photosensitizer, Rh-PMOF-**1** is powerful to catalyze CO_2 reduction to the formate ion with up to 99% selectivity, and can be recycled and reused for 3 runs. Theoretical study was further carried out to reveal the energy levels of the frontier orbitals of Rh-PMOF-**1** and the preferred binding sites of CO_2 in the framework.

1. Introduction

Our environment and life have been seriously influenced by anthropogenic CO_2 emission which arouses urgent demand for effective ways for the reduction of CO_2 concentration [1]. The report from the Intergovernmental Panel on Climate Change (IPCC) has suggested that the globally averaged combined land and ocean surface temperature shows a warming of 0.85 [0.65 to 1.06] ºC over the period 1880 to 2012. On the other hand, since the beginning of the industrial era, oceanic uptake of CO_2 has resulted in ocean acidification. The pH of ocean surface water has decreased by 0.1 (high confidence), corresponding to a 26% increase in acidity.

The conversion of CO_2 into valuable chemicals/fuels by solar energy is the most encouraging method to reduce the concentration of the greenhouse gas CO_2, considering that solar energy is the best clean and renewable energy [2]. MOFs possess high potential for photocatalytic CO_2 reduction, benefiting from their high CO_2 capture capacity. The structures and properties of MOFs can be elaborately tuned by incorporating homogeneously photocatalytic catalysts into the frameworks as either the connecting ligands or the nodes. Although a few molecular photocatalysts based on metal-polypyridine complexes, including $Re(CO)_3(bpy)Cl$, $Ru(bpy)(terpy)(CO)$, $Ru(CO)_2Cl_2(bpy)$, $Ru(bpy)_3$, $Cp^*Rh(bpy)Cl_2$ and $Ir(ppy)_2(bpy)$ (bpy = 2,2′-bipyridine, terpy = 2,2′:6′,2″-terpyridine, ppy = 2-phenylpyridine) have been incorporated into MOFs to afford photocatalysts for CO_2 reduction using visible light [3–8], the efficiency, selectivity and stability (especially low metal leaching and recyclability) are still critical issues as well as challenging problems (Tables S1 and S2). Rational design leading to a powerful MOF photocatalyst is highly demanded.

To achieve high efficiency, the photocatalyst should possess some important characteristics such as strong absorption of visible light and long lifetime of excited state. Porphyrins are well-known redox-active photosensitizers, most of which have the ability to absorb blue and red light corresponding to the Soret and Q-bands, respectively, and display remarkable long lifetime of the triplet excited state usually with a microsecond or even millisecond time scale [9]. Therefore, porphyrins are

* Corresponding authors.
E-mail addresses: zhli99@mail.sysu.edu.cn (L. Zhang), cesscy@mail.sysu.edu.cn (C.-Y. Su).

https://doi.org/10.1016/j.apcatb.2018.02.055
Received 26 December 2017; Received in revised form 15 February 2018; Accepted 24 February 2018
Available online 03 March 2018
0926-3373/

potentially more efficient photosensitizers than metal-polypyridine complexes. Nevertheless, only a limited number of porphyrin-based metal-organic frameworks (PMOFs) have been applied in photocatalytic CO_2 reduction reaction [10,11].

The reduction of CO_2 can lead to a series of products with different carbon oxidation ranging from $HCOO^-$, CO, CH_3OH, to CH_4. So product selectively is another important issue to be carefully considered during photocatalytic CO_2 reduction process in order to reduce the cost of separation and purification [12]. Product selectivity can be achieved by turning the reaction parameters such as CO_2 adsorption mode, pH of the reaction solution, surface functional group, co-catalyst and so on. Although a number of MOF-based photocatalysts have been reported, most of them suffer from uncontrollable selectively.

Adequate thermal stability, typically above 250 °C, and chemical stability, especially in polar solvents and water, can largely assist MOFs with photocatalytic reactions. However, many reported MOFs are lack of good stability, and suffer from the collapse of framework after the catalytic reaction, resulting in serious metal leaching and non-recyclability. The breakthrough appears when the highly charged cations (*e.g.* Al^{3+}, Fe^{3+}, Zr^{4+} and Hf^{4+}) are successfully used as the metal nodes, leading to high thermal stability up to 500 °C, resisting water and even challenging acidic and basic aqueous solutions [13–17].

Herein, we report the first example of the rhodium(III)-porphyrin metal-organic framework (Rh-PMOF-**1**(Zr)), which has been prepared from a metalloporphyrin tetracarboxylic ligand Rh(TCPP)Cl (TCPP = tetrakis(4-carboxyphenyl)porphyrin) with $ZrCl_4$ (Fig. 1) [18,19]. The Rh-porphyrin moieties are regularly and uniformly dispersed in the lattice of the framework showing **she** net topology, which actually endows Rh-PMOF-**1** with the unique feature of single-site photocatalyst. To our delight, Rh-PMOF-**1** displays much longer lifetime and better CO_2 reduction performance than the homogeneous counterpart, and behaves as a truly heterogeneous catalyst with low metal leaching.

2. Experimental section

2.1. General

All the reagents in the present work were obtained from the commercial source and used directly without further purification. The ligand 5,10,15,20-tetrakis(4-methoxycarbonylphenyl)porphyrin ($TCPPCO_2Me$) was synthesized according to the literature [18,19]. The elemental analyses were performed with Perkin-Elmer 240 elemental analyzer. HRESI-MS was performed by using a Bruker Daltonics ESI-Q-TOF maXis4G. Infrared spectra on KBr pellets were collected with a Nicolet/Nexus-670 FT-IR spectrometer in the region of 4000-400 cm^{-1}. UV–vis spectra were tested on a Shimadzu/UV-3600 spectrophotometer. ^1H and ^{13}C NMR were recorded on Bruker AVANCE III 400MHz. PXRD patterns were recorded on SmartLab X-ray powder diffractometer (Rigaku Co.) at 40 kV and 30 mA with a Cu target tube. Thermogravimetric (TG) analyses were performed under an N_2 atmosphere at a heating rate of 10 °C min^{-1} by using a NETZSCH TG 209 system. X-ray photoelectron spectroscopy (XPS) was performed on a ULVAC PHI Quantera microprobe. Binding energies (BE) were calibrated by setting the measured BE of C 1s to 284.65 eV. Energy-dispersive X-ray spectroscopy was recorded on a JSM-6330F field emission scanning electron microscope combined with EDS. ICP spectroscopy was conducted on a Spectro Ciros Vision ICP-OES spectrometer that is equipped with vacuum optics covering the spectral range from 175 to 777 nm, plasma power, 1300 w; coolant flow, 15.00 L/min; auxiliary flow, 0.80 L/min; nebulizer 0.70 L/min. The sorption isotherms were measured with an Autosorb-iQ2-MP gas sorption analyzer (Quantachrome, USA). Fluorescence spectra were measured on an Edinburgh FLS980 Photoluminescence Spectrometer. Before the fluorescence emission test, the equivalent solid-state Rh(TCPP)Cl and Rh-PMOF-**1** samples were finely ground to avoid error. The photoluminence lifetime experiments were performed in the time-correlated single photo counting (TCSPC) methods by using a 406.5 nm picoseconds pulsed diode laser, or by the same spectrometer but with a μF900 Xe lamp. $^{13}CO_2$ (~99% of ^{13}C, ~3% ^{18}O) was purchased from Sigma Aldrich.

2.2. X-ray crystallography

The X-ray diffraction data was collected with an Agilent Technologies SuperNova X-ray diffractometer system equipped with Cu-kα radiation (λ = 1.54178 Å). The crystal was kept at 150.0(1) K during data collection. The structure was solved with the SIR2004 structure solution program integrated in Olex2 using Direct Methods, and refined with the XH refinement package using CGLS minimization [20a]. The final refinement was performed by SHELXL-2014/7 (Sheldrick,) imbedded in WINGX [20b]. ISOR/SIMU was applied to all non-hydrogen atoms to simulate isotropic behaviors. Even though, ADP max/min ratios, especially for Rh and Zr atoms, are not prevented because of the difficulty to handle trivial disorder problem in highly symmetric space group. All solvent molecules have been removed by SQUEEZE program [20c]. The positions of the hydrogen atoms are generated geometrically. A summary of the crystal structure refinement data and selected bond angles and distances are listed in Tables S3, S4, S8 and S9. Crystallographic data for the structure have been deposited in the Cambridge Crystallographic Data Center with CCDC reference numbers 1470276 and 1454131.

2.3. Synthesis of Rh(TCPP)Cl

Rhodium porphyrin complex Rh($TCPPCO_2Me$)Cl was prepared according to a similar procedure [19]: $TCPPCO_2Me$ (168.2 mg, 0.2 mmol) and $RhCl_3$ (104.2 mg, 0.8 mmol) in PhCN (5 mL) was stirred at 190 °C. After 1 day, PhCN was removed by column chromatography on silica gel eluting with petrol. The crude reaction mixture was purified on

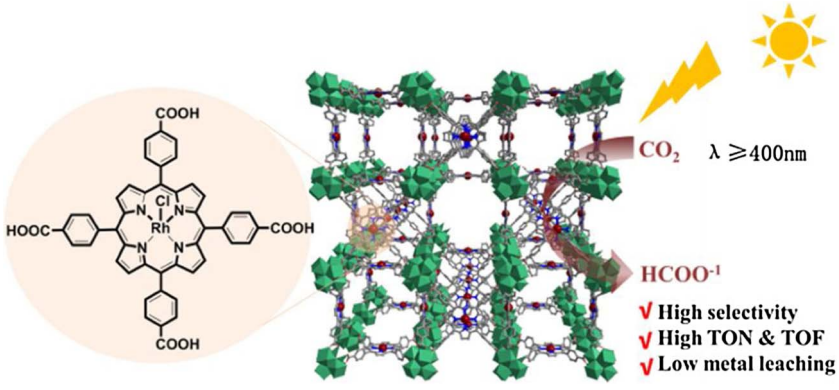

Fig. 1. Representation of catalytic behaviors of Rh-PMOF-**1**.

silica using a mixture of DCM and EtOAc as the eluent to afford the product as a red solid (145 mg, 76% yield based on $TCPPCO_2Me$). ^1H NMR (400 MHz, $CDCl_3$) δ 8.92 (s, 8H), 8.50-8.42 (m, 8H), 8.41-8.37 (m, 4H), 8.25-8.21 (m, 4H), 4.11 (s, 12H). FT-IR (KBr) ν 3426 (br), 2961 (s), 1725 (s), 1606 (s), 1433 (m), 1272 (s), 1110 (S), 1013 (s), 798 (w), 761 (m), 709 (m) cm^{-1}. HRMS (EI) *m/z* calcd. for $[C_{52}H_{36}N_4O_8RhCl\text{-}Cl]^+$: 947.1583, found: 947.1567. Anal. Calcd. For $C_{56}H_{47}ClN_4O_{11.5}Rh$ (Rh(TCPPCO$_2$Me)Cl·1.5H$_2$O·EtOAc): C, 61.24; H, 4.31; N, 5.10%. Found: C, 61.07; H, 3.97; N, 4.98. UV–vis (THF, λ_{max}, (logε)) 420.5 nm (5.32), 532 nm (4.34).

Rh(TCPP)Cl was prepared via the hydrolysis of the obtained Rh(TCPPCO$_2$Me)Cl according to a similar procedure: The obtained ester (120 mg) was stirred in a mixture of THF (6 mL) and MeOH (6 mL), to which a solution of KOH (100 mg) in H_2O (6 mL) was added. This mixture was refluxed for 5 h. After the reaction mixture was cooled down to room temperature, the organic solvents were removed under reduced pressure. The crude product as red precipitate was obtained after 1 M HCl was added to the aqueous suspension. Until no more precipitate was detected (pH ~ 2), the crude product was collected, washed with water (60 mL), and dried in vacuum. The yield is 90 mg (81%).^1H NMR (400 MHz, DMSO-d_6) δ 8.65 (m, 8H), 8.38 (m, 8H), 8.28 (m, 8H). ^{13}C NMR (100 MHz, DMSO-d_6) δ 167.47, 145.88, 141.64, 134.04, 133.88, 131.65, 130.21, 127.82, 127.71, 120.51. FT-IR (KBr) ν 3432 (br), 1692 (s), 1604 (s), 1406 (m), 1261 (s), 1076 (m), 1009 (s), 796 (s), 714 (m) cm^{-1}. HRMS (EI) *m/z* calcd. for $[C_{48}H_{28}N_4O_8RhCl\text{-}Cl]^+$: 891.0957, found: 891.0973. Anal. Calcd. for $C_{54.7}H_{41.4}Cl_{6.4}N_4O_{10}Rh$ (Rh(TCPP)Cl·2.7CH$_2$Cl$_2$·EtOAc): C, 52.79; H, 3.35; N, 4.5%. Found: C, 52.68; H, 3.54; N, 4.91%. UV–vis (THF, λ_{max}, (log ε)) 420.5 nm (5.23), 527 nm (4.29).

2.4. Synthesis of [($Zr_6(\mu_3\text{-}O)_8(OH)_2(H_2O)_{10})_2$(Rh(TCPP)Cl)$_3$] (Rh-PMOF-1(Zr))

Rh(TCPP)Cl (6 mg, 5.9×10^{-3} mmol), $ZrCl_4$ (10 mg, 0.04 mmol), benzoic acid (300 mg, 2.45 mmol), acetic acid (CH_3COOH, 0.3 mL), and dimethylformamide (DMF, 1 mL) were placed in a glass vial, which was then sealed and heated to 120 °C in an oven. After 48 h, red block crystals were obtained (6 mg, 64% yield based on Rh(TCPP)Cl) and air-dried. Anal Calcd For [($Zr_6(\mu_3\text{-}O)_8(OH)_2(H_2O)_{10})_2$(Rh(TCPP)Cl)$_3$]·19($C_6H_5COOH$)·11DMF·13$H_2O$ ($C_{310}H_{295}Cl_3Rh_3N_{23}O_{129}Zr_{12}$): C, 47.09%; H, 4.25%; N, 4.07%. Found: C, 47.03%; H, 3.873%; N, 4.05%. FT-IR (KBr) ν 3428 (br), 2917 (s), 1631 (s), 1403 (s), 1099 (m) cm^{-1}.

2.5. Photocatalytic reaction

In a 25 mL glass flask was placed the mixture of catalyst (10 mg), MeCN and TEOA solution (5 mL, v/v: 4/1), and pre-degassed with CO_2 to remove the dissolved O_2. Afterward, the flask was degassed with a pure CO_2 gas by bubbling through the reaction mixture over 5 min. Then the solution was irradiated with a 300 W Xe lamp with a UV-cut filter (Perfect Light) to remove light with wavelengths less than 400 nm. The $HCOO^-$ formed was detected by IC (882 Compact IC plus, Metrohm) with Metrosep A supp 4-250/4.0 column. The column temperature was maintained at 303 K. A mixture of 3.2 mM Na_2CO_3 and 1.0 mM $NaHCO_3$ was used as the eluent. The amount of H_2 in the gaseous phase was determined by GC (TCD), and those of CO and CH_4 were determined by GC (FID).

2.6. Isotopic tracing experiment

In a 25 mL glass flask was placed the mixture of Rh-PMOF-**1** (10 mg), CD_3CN and TEOA solution (5 mL, v/v: 4/1), and pre-degassed with $^{13}CO_2$ to remove the dissolved air. Afterward, the flask was degassed with a pure $^{13}CO_2$ (~99% of ^{13}C) gas by bubbling through the reaction mixture over 2 min. Then the solution was irradiated with a 300 W Xe lamp with a UV-cut filter (Perfect Light) to remove light with wavelengths less than 400 nm. After 18 h, the MOFs were collected via centrifugation and the supernatant was directly transferred to an NMR tube.

2.7. ICP spectrometric evaluation of metal leaching

The reaction mixture after 18 h was passed through a sand core funnel (G5) with a pad of celite, and washed with DCM. To examine the leached Rh content from the MOF catalyst Rh-PMOF-**1** into the reaction solution, the combined filtrate was concentrated to dryness. Afterward, the dryness was treated with aqua regia (4 mL) and aqueous hydrogen peroxide (30 wt%, 1 mL). The whole mixture was allowed to stay at room temperature for 2 h and heated at 150 °C to reduce the total volume to about 0.5 mL (If possible, the digestion procedure might be repeated twice). The resulted solution was diluted volumetrically with an aqueous solution of nitric acid (2%) to 25 mL, which was then evaluated by inductively coupled plasma optical emission spectrometer (ICP-OES) for Rh contents. The Rh content was measured in ppm (mg L^{-1}) based on calibration curves obtained with a series of calibration standard solutions doped with different amount of Rh. As for Rh-PMOF-**1** catalyzed CO_2 reduction reaction, the measured Rh content was 0.24 ppm (0.006 mg), corresponding to 0.9% leaching of Rh.

2.8. Computational details

All the calculations are accomplished with Gaussian 09 package [21]. The meta hybrid xc-functional M06 is employed with the basis set, consisting of quadruple zeta quality basis set Def2QZVP for Rh and 6-31G (d) basis set for C, H, N, O and Cl [22–25]. Geometry optimization is performed considering solvent effect as CH_3CN which is implicitly described by conductor-like polarizable continuum model (CPCM) method [26–28]. The composition of orbital is analyzed by Multiwfn 3.3.8, which is also an approach to explain the phenomenon induced by photon [29]. Meanwhile, Time-Dependent Density Functional Theory (TD-DFT) has been carried out to obtain the vertical excitation energy [30]. The first 30 excited singlet states are under consideration in the calculation of adsorption spectra for precise result.

Canonical Monte Carlo is a classical available simulation which depicts the process of a certain number of plural particles eventually achieves equilibrium after massive steps with constant temperature and pressure. Under the surrounding mutual interaction, atoms move randomly to generate a relative stable conformation. The number of 1×10^8 steps is applied in both equilibrium and production. The temperature to supply the intrinsic kinetic energy is 298.15 K, while the cut-off radius to completely non-repeatedly calculate the non-bonded interaction is 19.55 Å. All simulations are performed with the module of Sorption in Materials Studio 6.1 (San Diego, CA) using hybrid force-field [31]. A $4 \times 1 \times 1$ supercell is built for all simulation and calculation. The parameters of the adsorbates have been carefully studied in some force-field, and CO_2 has also been investigated by TraPPE [32]. The force-field has been employed to describe the interaction of multiple atoms, in which the metal and non-metal atom parameters are attributed to Universal Force Field (UFF) and DREIDING, respectively [33,34]. The Lennard-Jones parameters of the elements in the simulation are listed in Table S19. The charges can be obtained with the functional of GGA-PBE and a double numerical plus polarization version 4.4 (DNP) basis set in the module of DMol3. They can define electrostatic force which is summed by Ewald method [35–37]. DFT semi-core pseudopots are selected to treat core electrons.

3. Results and discussion

3.1. Synthesis and crystal structure

The ester-functionalized porphyrin, tetramethyl 4,4′,4″,4‴-(porphyrin-5,10,15,20-tetrayl)tetrabenzoate ($TCPPCO_2Me$) was prepared

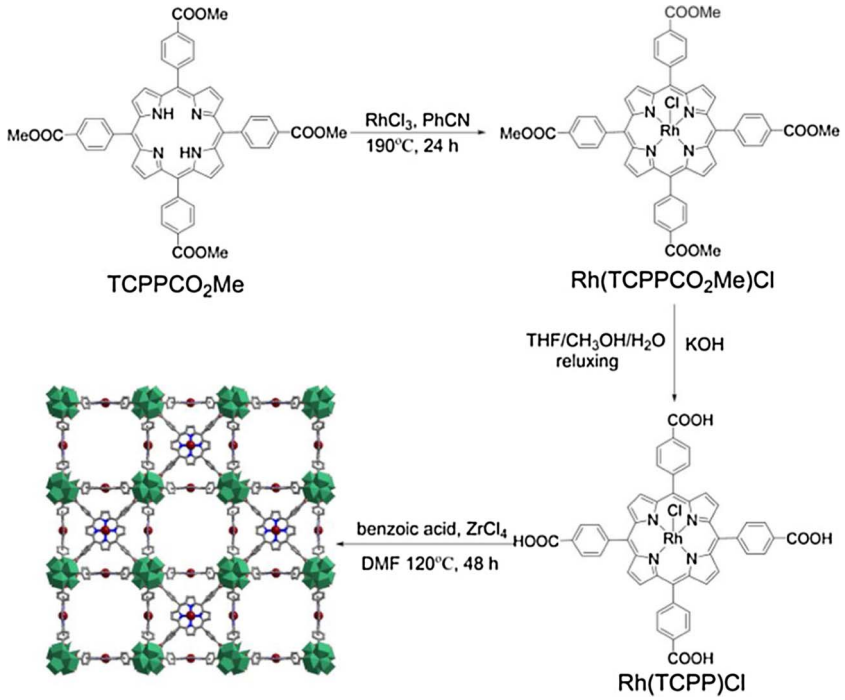

Fig. 2. Syntheses of metalloporphyrin ligands and Rh-PMOF-**1**.

according to the reported procedure, in which pyrrole and methyl 4-formylbenzoate were heating in propionic acid at 140 °C for 12 h (Fig. 2) [38]. Rh(TCPPCO$_2$Me)Cl was synthesized by the reaction of the porphyrin TCPPCO$_2$Me and RhCl$_3$ in the molar ratio of 1:4 and in benzonitrile (PhCN) at 190 °C for 1 day [19]. The structure of Rh(TCPPCO$_2$Me)Cl with an unsaturated five-coordination mode of the Rh center has been confirmed by the X-ray single crystallography (Figure S2), and the crystal structure refinement data and selected bond angles and distances are listed in Table S3 and S4, respectively. Afterwards, the hydrolysis of Rh(TCPPCO$_2$Me)Cl in KOH solution affords the Rh(TCPP)Cl, in which the Cl atom is still bound to Rh center as suggested by the energy-dispersive X-ray spectroscopy (EDS) analysis (Figure S3 and Table S5).

The assembly of ZrCl$_4$ and Rh(TCPP)Cl in the presence of benzoic acid at 120 °C for 48 h afforded red block crystals of Rh-PMOF-**1**(Zr) with the formula of $[(Zr_6(\mu_3\text{-}O)_8(OH)_2(H_2O)_{10})_2(Rh(TCPP)Cl)_3]\cdot$solvents. Both EDS and X-ray photoelectron spectroscopy (XPS) analyses indicate that the atomic ratio of Zr : Rh is around 4:1 (Figures S6 and S7; Tables S6 and S7). The XPS spectrum exhibits two contributions, located at 310.1 and 314.6 eV, which can be assigned to $3d_{5/2}$ and $3d_{3/2}$ of Rh, respectively, which confirms the +3 valence nature of Rh [39].

Rh-PMOF-**1**(Zr) crystallizes in the *I*m-3m space group, which is an isostructure of PCN-224, Ir-PMOF-**1** and Ru-PMOF-**1** [18,19]. The framework consists of 6-connecting Zr_6O_8 octahedron clusters linked by 4-connecting Rh(TCPP)Cl ligand, whereas all of the triangular faces of the Zr_6O_8 octahedron are capped by a μ_3-O atom. There are three dimensional channels (1.9 × 1.9 nm^2, atom-to-atom distances across opposite Rh atoms) in three orthogonal directions. Furthermore, the bigger cavities surrounded by 8 $Zr_6(\mu_3\text{-}O)_8$ clusters (3.0 × 3.0 × 3.0 nm^3) can be found in the framework, which are shown as the yellow ball in Fig. 3. The bulk purity of the as-prepared Rh-PMOF-**1** is confirmed by the powder X-ray different (PXRD) patterns which fit well with the simulated one from the single-crystal structure (Figure S8). To the best of our knowledge, Rh-PMOF-**1**(Zr) is the first example incorporating rhodium porphyrin units into metal-organic frameworks, which is of interest for practical applications due to the presence of single-sited unsaturated Rh-porphyrin units.

3.2. Stability, surface area and porosity

Excellent stability, high surface area and high porosity are of benefit to catalytic applications of MOFs. Rh-PMOF-**1** exhibits good thermal stability as evidenced by the high decomposition temperature up to 350 °C, which is disclosed by the thermal gravimetric (TG) curves of the fresh as well as activated samples (Figure S9). The thermal stability of Rh-PMOF-**1** has been further explored by the variable temperature VT-PXRD measurement, which suggests that the framework can be maintained up to 270 °C (Fig. 4). Moreover, Rh-PMOF-**1** possesses good chemical stability. After the crystalline samples were soaked in common solvents such as hexane, dichloromethane (DCM), acetone, acetonitrile (MeCN), isopropanol (^{i}PrOH) and water (H$_2$O) for one week, the PXRD tests suggest that Rh-PMOF-**1** retains good crystallinity upon these solvent treatments (Figure S10).

The permanent porosity of Rh-PMOF-**1** has been evaluated by N$_2$ adsorption isotherms at 77 K (Figure S11). Prior to sorption measurement, the samples were subjected to solvent exchange with acetone for 10 h and then activated by heating at 120 °C under vacuum for 12 h. The N$_2$ adsorption of Rh-PMOF-**1** shows the typical type I isotherms with N$_2$ uptakes of ~927 cm^3/g at 1 bar. The calculated Brunauer-Emmett-Teller surface area and pore volume are 3091 m^2 g^{-1} and 1.42 cm^{3}g^{-1}, respectively. In comparison, the theoretical BET surface and pore volume of Rh-PMOF-**1** are calculated by Material Studio to be 3279 m^2 g^{-1} and 1.03 cm^{3}g^{-1}, respectively [40]. As calculated by PLATON analysis, the effective solvent accessible void in the crystal lattice is 79% of the cell volume [41]. The porosity of Rh-PMOF-**1** has been further verified by the dye uptake test. Two organic dyes, i.e. orange G (OG, 15.6 × 10.1 × 5.4 Å^3) and methylene blue (MB, 16.3 × 7.9 × 4.0 Å^3), are chosen for the adsorption measurements [42]. After 24 h, around 84% of OG (67 mg g^{-1}, the adsorption amount of the dye per gram of the Rh-PMOF-**1**) or 38% of MB (24 mg g^{-1}) can be absorbed into the cavities of Rh-PMOF-**1** (Figure S12).

3.3. Gas adsorption

Effective adsorption and activation of CO$_2$ is a key step for improving the efficiency for CO$_2$ reduction, and besides, the CO$_2$

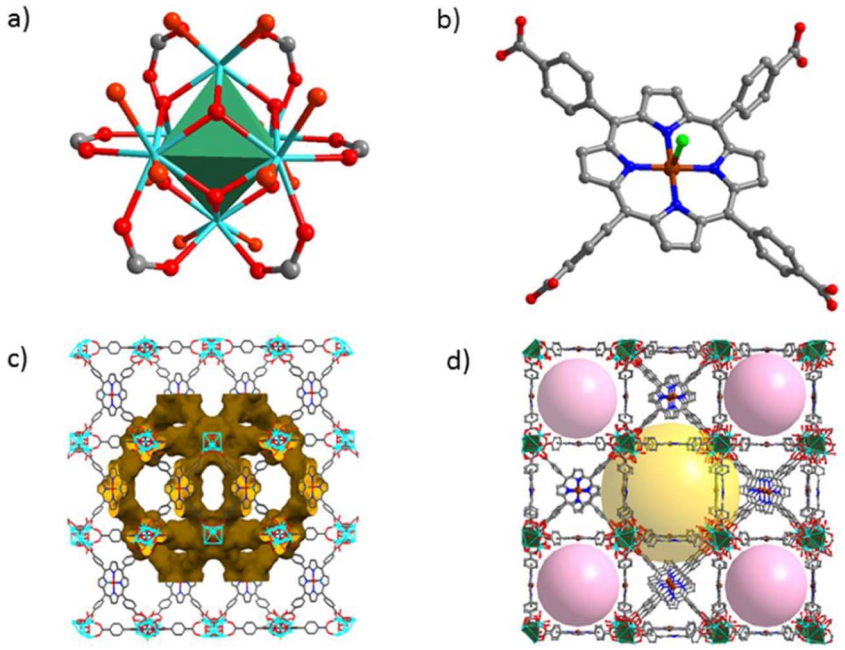

Fig. 3. Crystal structures of Rh-PMOF-**1**(Zr): (a) 6-connecting Zr_6O_8 cluster; (b) Rh(TCPP)Cl; (c,d) 3D views (the axil Cl atom are omitted for clarity). Rh (brown), N (blue), O (red), Cl (bright green) and C (gray).

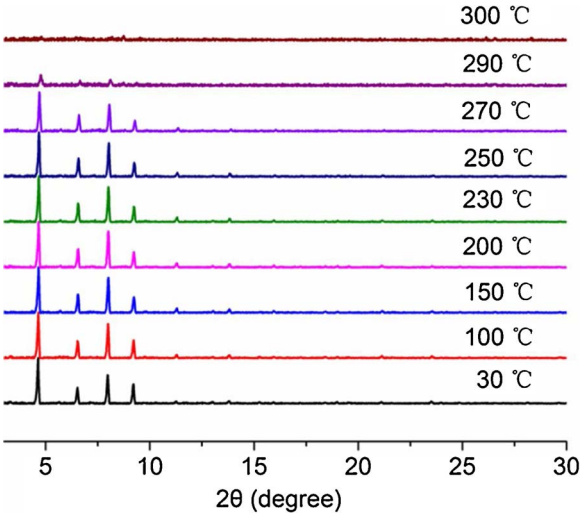

Fig. 4. Variable-temperature PXRD patterns of Rh-PMOF-**1** from 30 to 300°C.

adsorption configurations play an important role in the product distribution [43]. The CO_2 adsorption-desorption isotherms of Rh-PMOF-**1** at different temperatures disclose that it shows CO_2 uptake of 42, 53, 98 and 369 cm^3g^{-1} at 308, 298, 273 and 195 K, respectively, under 1 atm (Fig. 5). The CO_2 capacity of Rh-PMOF-**1** under ambient temperature (298 K) is higher than that of PCN-222 (35 cm^3/g) and Zr-bpdc /Ru(bpydc)(terpy)(CO)]$(PF_6)_2$ (23 cm^3/g), which have been previously employed as heterogeneous catalysts for CO_2 reduction [8,11].

As the dominant products of CO_2 photo-reduction reaction at less negative potentials, the local concentration of CO and H_2 molecules around the catalytically active centers will also influence the reaction pathways as well as the product distribution [44]. As for the metal-based catalysts, in which CO is more easily desorbed, the predominant reduction product often is CO. Rh-PMOF-**1** can absorb as high as 365 and 304 cm^3g^{-1} of CO and H_2 gases, respectively, at 77 K and 1 bar. We have further carried out the CO and H_2 sorption examination for Rh-PMOF-**1**(Zr) at 298 K, which shows that Rh-PMOF-**1**(Zr) can absorb 11 cm^3g^{-1} of CO but a negligible amount of H_2 at 298 K (Figure S11).

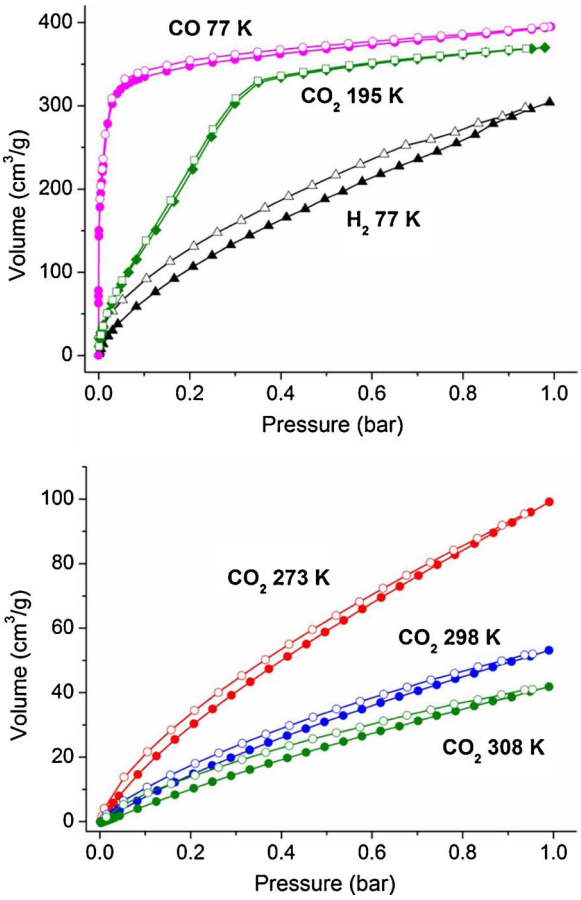

Fig. 5. H_2, CO and CO_2 gas adsorption-desorption isotherms of Rh-PMOF-**1**.

Considering that Rh-PMOF-**1** shows good adsorption capacity towards CO at low temperature as well as modest adsorption capacity at ambient temperature, we could draw a conclusion that Rh-PMOF-**1** might not prefer the reactions leading to the formation of CO as the major product [12,44].

3.4. Photophysical properties

The solid-state UV–vis absorption spectra indicate that both Rh(TCPP)Cl and Rh-PMOF-**1** exhibit high visible-light harvesting capability with the absorption edge extending to around 750 nm, which is crucial for photo-catalytic applications (Figure S14). In the THF solution, the UV–vis spectrum of Rh(TCPP)Cl includes a Soret band (B(0,0), 415 nm) and a Q band (Q(1,0), 527 nm), whose molar absorption coefficients are 2.06×10^5 and 1.96×10^4 $M^{-1}cm^{-1}$, respectively (Figure S15).

The excitation spectra and steady-state photoluminescence (PL) spectroscopy were also recorded to characterize the photophysical behaviors of Rh(TCPP)Cl metalloligand and Rh-PMOF-**1** (Figures S16). Upon excitation, Rh(TCPP)Cl shows two main PL peaks at about 651 and 715 nm, whereas in Rh-PMOF-**1** the emission bands are relatively red-shifted. In addition, when the equivalent of Rh-PMOF-**1** and Rh(TCPP)Cl is used for measurements, the emission intensity of the former is largely reduced compared to that of the latter, which indicates that the recombination rate of photo-generated electron-hole pairs are decreased after the integration of the Rh-porphyrin units into the framework (Fig. 6) [45].

One remarkable feature of Rh(TCPP)Cl and its MOF Rh-PMOF-**1** is their long-lived excited-states with the lifetime of 6 and 207 μs, respectively, at 298 K under vacuum, which is significant for an effective photocatalyst (Table 1 and S10-12) [7,46]. The luminescence decays of both Rh(TCPP)Cl and Rh-PMOF-**1** are well fitted to tri-exponential curves (Figures S17-19). For comparison, the metal-free porphyrin-based counterpart MOF of PCN-224 only displays much shorter lifetime of 1.7 ns under the same conditions. It is therefore concluded that, with the introduction of the noble metal of Rh(III) into the porphyrin ring and further integration of the Rh-porphyrin metalloligand into the framework, the excited-state lifetime of the resulting PMOFs could be largely elongated from the ns scale to the μs range. The lifetime of Rh-PMOF-**1** examined in the air at 298 K is found to be 13 μs, which is most probably quenched by O_2 due to the formation of the singlet oxygen, suggesting that the excited state of Rh-PMOF-**1** is largely triplet in character [47].

Metalloporphyrins with room-temperature phosphorescence (RTP) emission, especially Pt(II)- and Pd(II)-porphyrins, have been thoroughly studied over the past few decades. The mechanism of RTP emission of Pd- and Pt-porphyrins can be explained as the following: a significant contribution of the central metal d-orbitals to E_g molecular orbitals with D_{4h} symmetry has been achieved by the heavy-atom effect of the Pd or Pt ions, resulting in the high rates of intersystem crossing from their lowest excited singlet (S_1) state to the lowest triplet state (T_1), from which the metalloporphyrins decay by emitting phosphorescence [48–50]. The triplet state lifetimes of Pt- and Pd-porphyrins at room temperature are typically in the order of tens to hundreds of microseconds (μs). The RTP emissions of other platinum group metal-based porphyrin complexes have remained much less unexplored. In some cases, the Ir(III)-porphyrin complexes have been reported to be strong room-temperature emitters, and their triplet lifetimes at room temperature are in the range of 26–108 μs, based on different porphyrin and axial ligands [51,52] As for Rh(III)-porphyrin complexes, the phosphorescence at 77 K (liquid nitrogen temperature) have been observed [53], however, the RTP of Rh(III)-porphyrins has not been discovered yet. To the best of our knowledge, our work represents the first report about the RTP of Rh(III)-porphyrin complexes, revealing a similar RTP behavior as the Pt(II)- and Pd(II)-porphyrins. Specifically, the triplet state lifetime could be significantly elongated when incorporating the Rh(III)-porphyrin units into the metal-organic framework.

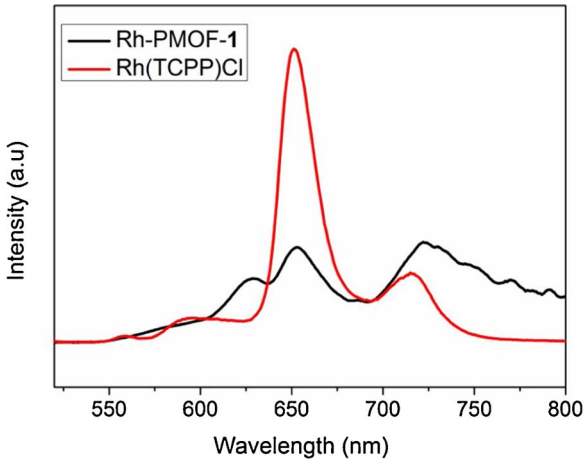

Fig. 6. Photoluminescence spectra of Rh(TCPP)Cl and Rh-PMOF-**1** excited at 376 nm.

Table 1
Emission Maxima and Lifetime Data[a].

Complex/MOF	Emission Max (nm)	Lifetime
Rh(TCPP)Cl	651, 715	6 μs (298 K) 18 μs (223 K) 41 μs (77 K) 4 μs (298 K)[b]
Rh-PMOF-**1**	654, 722	206 μs (298 K) 304 μs (223 K) 353 μs (77 K) 13 μs (298 K)[b]
PCN-224	654, 715	1.7 ns (298 K) 1.5 ns (223 K) 2.2 ns (77 K) 1.6 ns (298 K)[b]

[a] Rh(TCPP)Cl, Rh-PMOF-**1** and PCN-224 were excited at 420, 376 and 406.5 nm, respectively, and the data are based on the steady-state photoluminensce emission spectra in the vacuum.
[b] In the air.

3.5. Electrochemistry characterations

In order to evaluate the possibility of Rh-porphyrin-based complexes or PMOFs for CO_2 photo-reduction, the Mott–Schottky (M–S) plots were measured at frequencies of 500, 1000 and 1500 Hz, respectively. The positive slopes of the M-S plots are characteristic of *n*-type semiconductors (Figure S20) [54]. The flat band position determined from the intersection is approximately −0.77 V *vs.* Ag/AgCl (i.e. −0.57 V *vs.* NHE; −3.93 eV) for Rh-PMOF-**1** [55]. It has been proposed that the bottom of the conduction band (LUMO) in *n*-type semiconductors is approximately equal to the flat band potential [56], and then the LUMO of Rh-PMOF-**1** is estimated to be −0.57 V *vs.* NHE. In the similar way, the LUMO of Rh(TCPP)Cl and the metal-free PCN-224 is calculated to be -0.6 and −0.5 V *vs.* NHE), respectively (Figures S21 and S22). Compared to the non-metal porphyrin-based PCN-224, the Rh-porphyrin-containing Rh-PMOF-**1** displays slightly more negative LUMO potential.

To achieve the photocatalytic reduction of CO_2 thermodynamically, the LUMO of photocatalysts should have a more negative potential than CO_2 reduction potentials (e.g. $CO_2/HCOO^-$, −0.49 V; CO_2/CO, −0.51 V *vs.* NHE at pH = 7, Table S13) [57], in which the pH value is noted to has a significant effect on the redox potentials. Therefore, it is thermodynamically feasible for both Rh(TCPP)Cl and Rh-PMOF-**1** to behave as CO_2 reduction photocatalyts.

3.6. Photocatalytic activity

The photocatalytic reduction of CO_2 was carried out using acetonitrile and triethanolamine (TEOA) as the reaction solvent and

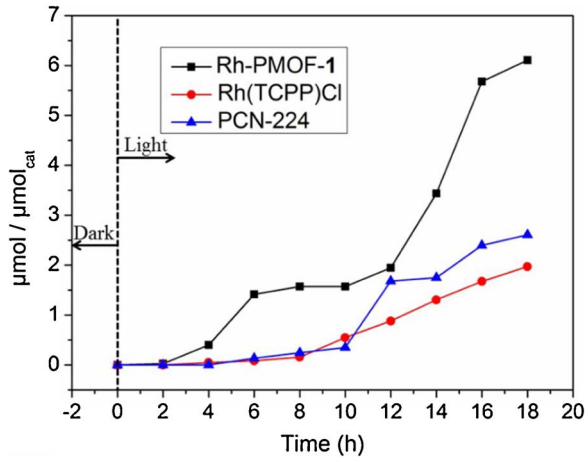

Fig. 7. The amount of $HCOO^{-1}$ (μmol/μmol$_{cat}$) produced in different reaction time.

sacrificial, respectively, under visible light irradiation (λ ≥ 400 nm) in the absence of additional photosensitizer. The reaction flask was degassed with a pure CO_2 gas by bubbling through the reaction mixture over 5 min, and the pH of the solution was 6 as determined by the pH meter. As shown in Fig. 7, Rh-PMOF-**1** shows excellent catalytic activity towards CO_2 reduction, leading to the formation of formate ion as sole product (Figure S25 and Table S15). A negligible amount of other products have been detected by either ion or the gas chromatograph. In comparison, Rh(TCPP)Cl and PCN-224 displays much poorer performances.

The amount of $HCOO^-$ increased with the reaction time, and reached 6.1 μmol/μmol$_{cat}$ in 18 h for Rh-PMOF-**1**. The turnover frequency (TOF) of Rh-PMOF-**1** for the photocatalytic reduction of CO_2 is calculated to be 0.34 h^{-1}, which is higher than those of the reported MOF-based photocatalysts such as NH_2-MIL-125(Ti), NH_2-Uio-66(Zr), PCN-222 and NNU-28 (0.044, 0.046, 0.14 and 0.22 h^{-1}, respectively), and comparable with that of best performed MOF-253-Ru$(CO)_2Cl_2$ (0.36 h^{-1}) (Table S2).[5,11a,58,59] To verify the source of the produced $HCOO^-$, we have carried out the isotopic tracing experiment using $^{13}CO_2$. The ^{13}C NMR spectrum of the product obtained from the reaction with $^{13}CO_2$ shows the two peaks corresponding to CD_3CN and TEOA, and three additional peaks being assigned to the dissolved $^{13}CO_2$, $H^{13}CO_3$- and $H^{13}COO^-$, respectively (Figure S23) [11,58a] In comparison, no $H^{13}COO^-$ product has been observed in the parallel reaction with normal CO_2 (Figure S24). In addition, a series of controlled experiments of CO_2 photo-reduction including in the nitrogen/oxygen atmosphere, in the dark, and without Rh-PMOF-**1** have been carried out, whereas catalytic results show that no $HCOO^-$ can be detected under these conditions (Table S14). Both the isotopic tracing and control experiments indicate that $HCOO^-$ is produced from photocatalytic reduction of CO_2.

On the other hand, product selectivity is one of the most important issues to be considered during photo-catalytic CO_2 reduction process. Formic acid and carbon monoxide are the two-electron reduction products of CO_2. According to the reaction mechanisms of the $2e^-$ reduction of CO_2 proposed by Zapol et al, the first step is the absorption of CO_2 and then its activation to form CO_2^- [43]. The possible adsorption configurations of CO_2 on the semiconductor surface have been reported, including carbon, oxygen and mixed coordination (Figure S26). As for the oxygen coordination mode, CO_2^- prefers to combine with a hydrogen atom to form a formate anion and then a proton to form formic acid, in which the cleavage of the C—O bond does not occur and formic acid may become the final product. With regards to carbon coordination mode, carbon monoxide is the major product when the photocatalyst has weak CO adsorption properties and the adsorbed CO can easily desorb from the surface of catalysts [12]. Considering that Rh-PMOF-**1** displays adequate adsorption capacity towards CO_2 and CO (Fig. 5 and S11), and the strong bonds between CO and Rh atoms have been found in a number of carbonyl rhodium porphyrin complexes such as RhCl(CO)(porphyrin) (porphyrin = tetraphenylporphyrin or octaethylporphyrin) [60], we guess that the CO_2^- might prefer to combine with a hydrogen atom to form a $HCOO^-$ anion, which might explain the highly selective production of $HCOO^-$ in our case. In comparison, the reported MOF photocatalysts incorporated with Re$(CO)_3$(bpy)Cl and Ru$(CO)_2Cl_2$ gave the major reduction product of CO (Table S1). It is noted that in the presence of additional photosensitizer (i.e. Ru$(bpy)_2Cl_2$), the major product was changed to $HCOO^-$ with the same catalyst of MOF-253-Ru$(CO)_2Cl_2$ [5].

The fairly high stability of Rh-PMOF-**1** makes it behave as a robust and truly heterogeneous photocatalyst. The crystalline catalysts can be isolated from the reaction mixture by centrifugation, and can be reused for 3 times without loss of activity (Table S17). Before each repeating run, Rh-PMOF-**1** catalyst was washed with acetone to remove the reaction solution in the interior and exterior surfaces. In the second run, the yield of $HCOO^{-1}$ decreased from 6.1 to 5.6 μmol/μmol$_{cat}$, whereas in the third run the yield increases up to 7.5 μmol/μmol$_{cat}$. The PXRD monitoring experiments before and after catalytic reactions show that the crystal framework of Rh-PMOF-**1** is remained after the photocatalytic reaction (Figure S27). After the third run, the framework structure remained but the crystallinity became poorer as suggested from the broadened and weakened PXRD patterns [61]. The XPS analyses confirm that the Rh atoms in the recycled MOF catalyst samples are still in + 3 valence, which is the same as that of the as-synthesized samples (Figure S28). Inductively coupled plasma optical emission spectrometer (ICP-OES) analysis of the filtrate after catalysis indicates that the amount of the Rh leaching into the reaction mixture is 0.9% of the total Rh content in Rh-PMOF-**1**.

In order to confirm the heterogeneous nature of Rh-PMOF-**1** catalyzed CO_2 reduction, the filtration experiment has been carried out as following: after photocatalysis in 18 h, the reaction mixture was filtered with a filtration membrane (0.45 μm) to remove the catalyst. To the filtrate was added TEOA (1 mL), the resulting solution was re-saturated with CO_2. The reaction mixture was allowed to under visible light irradiation (λ ≥ 400 nm) for another 18 h. Catalytic result showed that the filtrate was almost inactive (Table S18), suggesting that the leached Rh in the reaction solution can't account for the reactivity of Rh-PMOF-**1**.

3.7. Theoretical studies

Time-dependent density functional theory (TD-DFT) has been carried out to obtain the vertical excitation energy. To examine whether our calculation is reliable, the data were compared with the experimental results. As shown in Figure S29, the theoretical and experimental absorption spectra of TCPP and Rh(TCPP)Cl at the M06 levels were comparable, which confirmed the reliability of the calculation method.

The frontier orbitals are of vital importance for the discussion of the electronic distribution. The TCPP-Zr_6O_8 and Rh(TCPP)Cl-Zr_6O_8 composites, which are labeled as C1 and C2, respectively, have been considered in our computational studies instead of TCPP and Rh(TCPP)Cl, considering that the Zr_6O_8 clusters might have an influence on the photo-induced electron transfer (Figures S30). The electronic distributions of the frontier orbitals of C1 and C2 are centralized on the porphyrin ring whereas aren't related to the Zr_6O_8 cluster (Figures S31 and S32). As shown in Fig. 8 and Table S20, after the incorporation of the rhodium atom into the porphyrin ring, the energy levels of HOMO and LUMO of C2 are decreased compared to those of C1. It may be due to the formation of the conjugated π bond between the d orbital of the central Rh atom and the p orbital of the C or N atoms of the porphyrin ring, thereof the energy levels of the frontier orbitals of Rh(TCPP)Cl should be greatly reduced in comparison to TCPP. The LUMO energy levels of both C1 and C2 are above the energies corresponding to CO_2/

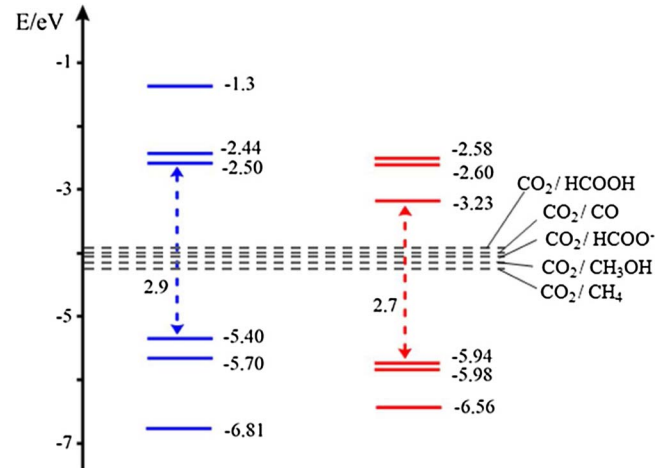

Fig. 8. The energy levels and HOMO–LUMO gaps of TCPP-Zr_6O_8 (C1, left) and Rh(TCPP)Cl-Zr_6O_8 composites (C2, right).

CH_xO_y levels. This means that the C1 or C2-based MOFs could be thermodynamically able to donate an excited electron from the conduction band for the CO_2 reduction half-reactions to proceed, which is consistent with our experimental results [62].

It is noted that, in comparison to HOMO, the energy level of the LUMO of C2 decreased more significantly. The HOMO-LUMO gaps of C1 and C2 are 2.9 and 2.7 eV, respectively. This might because the d_z^2 orbitals of Rh atom are involved in the formation of LUMO of C2, which contribute to LUMO more than to that of HOMO. As shown in Figure S32, the LUMO of C2 is composed of the d_z^2 orbital of the Rh atom, the p_z orbital of the N atom of the pyrrole, and a small amount of p_z orbital of C. Orbital composition analysis using Mulliken method also confirms this conclusion (Table S21).

Center-of-mass probability density plots of CO_2 molecules in Rh-PMOF-**1** can be obtained from the result of Monte Carlo simulation, which could disclose the nature of the CO_2–framework interactions. The CO_2 molecules adsorbed in the pores of Rh-PMOF-**1** are mainly distributed around the porphyrin rings and the Zr_6O_8 clusters due to non-bonded interactions between CO_2 molecules and μ_3-O atoms of Zr_6O_8 clusters or the O atoms of the coordinated water molecules (Fig. 9). The consistency of the preferred binding sites of CO_2 and the catalytic centers around the Rh-porphyrin units and the Zr_6O_8 clusters should assist the CO_2-related reactions to occur, which might explain the high activity of Rh-PMOF-**1** in CO_2 reduction reactions.

3.8. Reaction mechanism

Based on the above discussion, we proposed a possible reaction mechanism (Fig. 10): In Rh-PMOF-**1**(Zr), the rhodium-porphyrin unit acts as both an antenna to absorb visible light and a catalytic center. On one hand, upon irradiation, the metalloporphyrin ligand behaves as an antenna to absorb the visible light, gives rise to the excited state, and transfers electrons to the zirconium oxo clusters, reducing Zr(IV) to Zr (III) atoms, which is then able to reduce CO_2 to formate [58]. On the other hand, the rhodium-porphyrin ligand itself can act as photocatalytic centers and carry out the CO_2 reduction. The catalytic role of Rh centers can be confirmed from the performance comparison of Rh-PMOF-**1** and PCN-224 without the Rh centers towards CO_2 photocatalytic reaction, showing that the former is much more efficient than the latter (Fig. 7). In both pathways, TEOA behaves as the sacrificial agent to achieve a complete photocatalytic cycle. The above two catalytic pathways contribute simultaneously to the CO_2 photoreduction, giving rise to formate ions, and account for the high performance of Rh-PMOF-**1** [59].

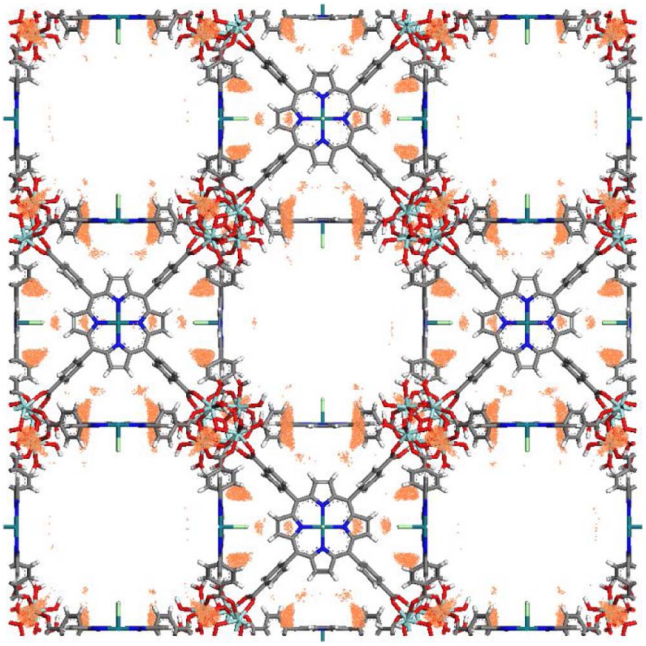

Fig. 9. Center-of-mass probability density plots of CO_2 molecules (presented as orange dots) in Rh-PMOF-**1** from the simulation. Probabilities along the *c* axis are summed and projected onto the *ab* plane. The density of dots indicates the probability of CO_2 molecules appearing in this space.

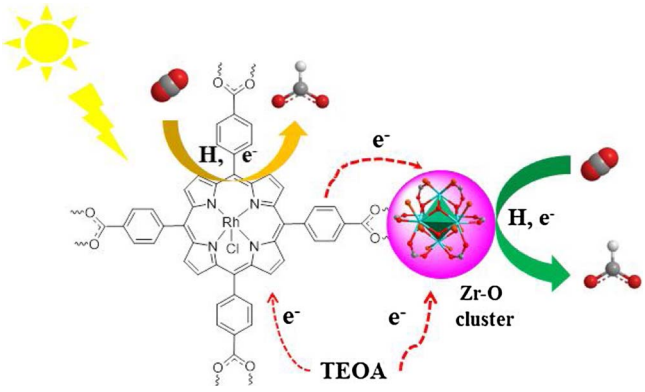

Fig. 10. The proposed photo-catalytic mechanism of dual catalytic centers in Rh-PMOF-**1**.

4. Conclusion

In summary, we have successfully synthesized a rhodium(III)-porphyrin-based metal-organic framework (Rh-PMOF-**1**(Zr)) for the first time, which is highly porous and stable. Thanks to the regularly and uniformly dispersed rhodium porphyrin moieties within the framework as well as the long excited state lifetime, Rh-PMOF-**1** shows efficient and selective behaviors (up to 99% selectivity) for CO_2 reduction compared to its homogeneous counterpart. Theoretical studies have further disclosed that the Rh-porphyrin-based materials are thermodynamically favorable for CO_2 reduction reactions to occur, and also suggest that the CO_2 adsorption sites are distributed around the Rh-porphyrin active centers. Further work about the design and catalytic applications of the noble metal porphyrin-based MOFs are in process.

Acknowledgment

This work was supported by the NSFC Projects (21773314, 21573291, 21720102007), the STP Project of Guangzhou (201707010168), and the Fundamental Research Funds for the Central Universities.

Appendix A. Supplementary data

Supplementary material related to this article can be found, in the online version, at doi:https://doi.org/10.1016/j.apcatb.2018.02.055.

References

[1] R. Pachauri, L. Meyer, Climate Change 2014 Synthesis Report, Intergovernmental Panel on Climate Change, 2015.
[2] (a) S.C. Roy, O.K. Varghese, M. Paulose, C.A. Grimes, ACS Nano 4 (2010) 1259–1278;
(b) T. Zhang, W. Lin, Chem. Soc. Rev. 43 (2014) 5982–5993;
(c) G.A. Ozin, Adv. Mater. 27 (2015) 1957–1963;
(d) L. Zeng, X. Guo, C. He, C. Duan, ACS Catal. 6 (2016) 7935–7947;
(e) A. Dhakshinamoorthy, A.M. Asiri, H. Garcia, Angew. Chem., Int. Ed. 55 (2016) 5414–5445;
(f) H. He, J.A. Perman, G. Zhu, S. Ma, Small 12 (2016) 6309–6324;
(g) Y. Huang, J. Liang, X. Wang, R. Cao, Chem. Soc. Rev. 46 (2017) 126–157.
[3] C. Wang, Z. Xie, K.E. deKrafft, W. Lin, J. Am. Chem. Soc. 133 (2011) 13445–13454.
[4] L. Li, S. Zhang, L. Xu, J. Wang, L. Shi, Z. Chen, M. Hong, J. Luo, Chem. Sci. 5 (2014) 3808–3813.
[5] D. Sun, Y. Gao, J. Fu, X. Zeng, Z. Chen, Z. Li, Chem. Commun. 51 (2015) 2645–2648.
[6] M.B. Chambers, X. Wang, N. Elgrishi, C.H. Hendon, A. Walsh, J. Bonnefoy, J. Canivet, E.A. Quadrelli, D. Farrusseng, C. Mellot-Draznieks, M. Fontecave, ChemSusChem 8 (2015) 603–608.
[7] S.Q. Zhang, L.N. Li, S.G. Zhao, Z.H. Sun, J.H. Luo, Inorg. Chem. 54 (2015) 8375–8379.
[8] T. Kajiwara, M. Fujii, M. Tsujimoto, K. Kobayashi, M. Higuchi, K. Tanaka, S. Kitagawa, Angew. Chem., Int. Ed. 55 (2016) 2697–2700.
[9] (a) S. Funyu, T. Isobe, S. Takagi, D. Tryk, H. Inoue, J. Am. Chem. Soc. 125 (2003) 5734–5740;
(b) P. Chen, O.S. Finikova, Z. Ou, S.A. Vinogradov, K.M. Kadish, Inorg. Chem. 51 (2012) 6200–6210;
(c) L. Hamon, M. Gouterman, J. Hanson, J. Am. Chem. Soc. 95 (1973) 4822–4829;
(d) M. Hoshino, H. Seki, K. Yasufuku, J. Phys. Chem. 90 (1986) 5149–5153;
(e) S.E. Vitols, D.A. Friesen, D.S. Williams, D. Melamed, T.G. Spiro, J. Phys. Chem. 100 (1996) 207–213;
(f) H. Suzuki, Y. Miyazaki, M. Hoshino, J. Phys. Chem. 107 (2003) 1239–1245;
(g) W.-Y. Gao, M. Chrzanowski, S. Ma, Chem. Soc. Rev. 43 (2014) 5841–5866.
[10] Y. Liu, Y. Yang, Q. Sun, Z. Wang, B. Huang, Y. Dai, X. Qin, X. Zhang, ACS Appl. Mater. Inter. 5 (2013) 7654–7658.
[11] (a) H.Q. Xu, J. Hu, D. Wang, Z. Li, Q. Zhang, Y. Luo, S.H. Yu, H.L. Jiang, J. Am. Chem. Soc. 137 (2015) 13440–13443;
(b) H. Zhang, J. Wei, J. Dong, G. Liu, L. Shi, P. An, G. Kong, J. Zhao, X. Wang, X. Meng, J. Zhang, J. Ye, Angew. Chem. Int. Ed 55 (2016) 14310–14314.
[12] (a) W. Tu, Y. Zhou, Z. Zou, Adv. Mater. 26 (2014) 4607–4626;
(b) X. Chang, T. Wang, J. Gong, Energy Environ. Sci. 9 (2016) 2177–2196.
[13] (a) Y. Bai, Y. Dou, L.H. Xie, W. Rutledge, J.R. Li, H.C. Zhou, Chem. Soc. Rev. 45 (2016) 2327–2367;
(b) M. Rimoldi, A.J. Howarth, M.R. DeStefano, L. Lin, S. Goswami, P. Li, J.T. Hupp, O.K. Farha, ACS Catal. 7 (2017) 997–1014.
[14] J.H. Cavka, S. Jakobsen, U. Olsbye, N. Guillou, C. Lamberti, S. Bordiga, K.P. Lillerud, J. Am. Chem. Soc. 130 (2008) 13850–13851.
[15] V. Guillerm, F. Ragon, M. Dan-Hardi, T. Devic, M. Vishnuvarthan, B. Campo, A. Vimont, G. Clet, Q. Yang, G. Maurin, G. Férey, A. Vittadini, S. Gross, C. Serre, Angew. Chem., Int. Ed. 51 (2012) 9267–9271.
[16] D. Feng, K. Wang, J. Su, T.-F. Liu, J. Park, Z. Wei, M. Bosch, A. Yakovenko, X. Zou, H.-C. Zhou, Angew. Chem., Int. Ed. 54 (2015) 149–154.
[17] T.C. Wang, W. Bury, D.A. Gomez-Gualdron, N.A. Vermeulen, J.E. Mondloch, P. Deria, K. Zhang, P.Z. Moghadam, A.A. Sarjeant, R.Q. Snurr, J.F. Stoddart, J.T. Hupp, O.K. Farha, J. Am. Chem. Soc. 137 (2015) 3585–3591.
[18] D. Feng, W.-C. Chung, Z. Wei, Z.-Y. Gu, H.-L. Jiang, Y.-P. Chen, D.J. Darensbourg, H.-C. Zhou, J. Am. Chem. Soc. 135 (2013) 17105–17110.
[19] (a) Y. Wang, H. Cui, Z. Wei, H. Wang, L. Zhang, C.-Y. Su, Chem. Sci. 8 (2017) 775–780;
(b) H. Cui, Y. Wang, Y. Wang, Y.-Z. Fan, L. Zhang, C.-Y. Su, CrystEngComm 18 (2016) 2203–2209;
(c) L. Chen, H. Cui, Y. Wang, X. Liang, L. Zhang, C.-Y. Su, Dalton Trans. (2018), http://dx.doi.org/10.1039/C8DT00434J.
[20] (a) O.V. Dolomanov, L.J. Bourhis, R.J. Gildea, J.A.K. Howard, H. Puschmann, J. Appl. Cryst. 42 (2009) 339–341;
(b) L.J. Farrugia, J. Appl. Cryst. 32 (1999) 837–838;
(c) P.V.D. Sluis, A.L. Spek, Acta Cryst. Sect. A 46 (1990) 194–201.
[21] M.J. Frisch, et al., Gaussian 09, Revision A.02, Gaussian, Inc, Wallingford, CT, 2009.
[22] Y. Zhao, D.G. Truhlar, Theor. Chem. Acc. 120 (2008) 215–241.
[23] F. Weigend, R. Ahlrichs, Phys. Chem. Chem. Phys. 7 (2005) 3297–3305.
[24] F. Weigend, Phys. Chem. Chem. Phys. 8 (2006) 1057–1065.
[25] J.A. Montgomery, J. Chem. Phys. 94 (1991) 6091–6101.
[26] S. Miertuš, E. Scrocco, J. Tomasi, Chem. Phys. 55 (1981) 117–129.
[27] M. Cossi, V. Barone, R. Cammi, J. Tomasi, Chem. Phys. Lett. 255 (1996) 327–335.
[28] V. Barone, M. Cossi, J. Phys. Chem. A. 102 (1998) 1995–2001.
[29] T. Lu, F.W. Chen, J. Comput. Chem. 33 (2012) 580–592.
[30] G. Scalmani, M.J. Frisch, B. Mennucci, J. Tomasi, R. Cammi, V.J. Barone, Chem. Phys. 124 (2006) 094107.
[31] K.F. Khaled, J. Appl. Electrochem. 41 (2011) 423–433.
[32] J.J. Potoff, J.I. Siepmann, AIChE J. 47 (2001) 1676–1682.
[33] A.K. Rappé, C.J. Casewit, K.S. Colwell, W.A. Goddard III, W.M. Skiff, J. Am. Chem. Soc. 114 (1992) 10024–10035.
[34] S.L. Mayo, B.D. Olafson, W.A. Goddard III, J. Phys. Chem. 94 (1990) 8897–8909.
[35] J.P. Perdew, K. Burke, M. Ernzerhof, Phys. Rev. Lett. 77 (1996) 3865–3868.
[36] B. Delley, J. Phys. Chem. A. 110 (2006) 13632–13639.
[37] P.P. Ewald, Ann. Phys. 64 (1921) 253–287.
[38] D. Feng, Z.Y. Gu, J.R. Li, H.L. Jiang, Z. Wei, H.C. Zhou, Angew. Chem., Int. Ed. 51 (2012) 10307–10310.
[39] J.P. Contour, G. Mouvier, M. Hoogewys, J. Catal. 48 (1977) 217–228.
[40] T. Düren, F. Millange, G. Férey, K.S. Walton, R.Q. Snurr, J. Phys. Chem. C 111 (2007) 15350–15356.
[41] A.L. Spek, J. Appl. Crystallogr. 36 (2003) 7–13.
[42] X. Zhao, X. Bu, T. Wu, S.T. Zheng, L. Wang, P. Feng, Nat Commun. 4 (2013) 2344.
[43] H. He, P. Zapol, L.A. Curtiss, Energy Environ. Sci. 5 (2012) 6196–6205.
[44] M. Gattrell, N. Gupta, A. Co, J. Electronal. Chem. 594 (2006) 1–19.
[45] (a) S. Bai, J. Jiang, Q. Zhang, Y.J. Xiong, Chem. Soc. Rev. 44 (2015) 2893–2939;
(b) C. Gao, J. Wang, H. Xu, Y. Xiong, Chem. Soc. Rev. 46 (2017) 2799–2823.
[46] (a) J. Yang, Z. Wang, Y. Li, Q. Zhuang, J. Gu, Chem. Mater. 28 (2016) 2652–2658;
(b) S. Zhang, L. Li, S. Zhao, Z. Sun, M. Hong, J. Luo, J. Mater. Chem. A 3 (2015) 15764–15768.
[47] H.M. Zhao, L.X. Zang, H. Zhao, F. Qin, Z.W. Li, Z.G. Zhang, W.W. Cao, J. Phys. Chem. C 119 (2015) 10558–10563.
[48] O.S. Finikova, A.V. Cheprakov, S.A. Vinogradov, J. Org. Chem. 70 (2005) 9562–9572.
[49] P.P. Pershukevich, V.A. Galievsky, A.S. Stasheuski, E.A. Makarova, E.A. Luk'yanets, K.N. Solovyov, J. Appl. Spectr. 77 (2011) 790–801.
[50] L.X. Zang, H.M. Zhao, J.Y. Hua, W.W. Cao, F. Qin, J.T. Yao, Y. Tian, Y.D. Zheng, Z.G. Zhang, J. Mater. Chem. C. 4 (2015) 9851–9857.
[51] K. Koren, S.M. Borisov, R. Saf, I. Klimant, Eur. J. Inorg. Chem. (2011) 1531–1534.
[52] K. Koren, R.I. Dmitriev, S.M. Borisov, D.B. Papkovsky, I. Klimant, ChemBioChem. 13 (2012) 1184–1190.
[53] D.B. Papkovsky, T.C. O'Riordan, J. Fluoresc. 15 (2005) 569–584.
[54] R.M. Fernández-Domene, E. Blasco-Tamarit, D.M. García-García, J. García Antón, J. Electrochem.Soc. 161 (2014) C25–C35.
[55] D.K. Kanan, E.A. Carter, J. Phys. Chem. C 116 (2012) 9876–9887.
[56] Z. Zhang, J. Long, L. Yang, W. Chen, W. Dai, X. Fu, X. Wang, Chem. Sci. 2 (2011) 1826–1830.
[57] (a) S. Xie, Q. Zhang, G. Liu, Y. Wang, Chem. Commun. 52 (2016) 35–59;
(b) J. Schneider, H. Jia, J.T. Muckerman, E. Fujita, Chem. Soc. Rev. 41 (2012) 2036–2051;
(c) M.D. Doherty, D.C. Grills, J.T. Muckerman, D.E. Polyansky, E. Fujita, Coord. Chem. Rev. 254 (2010) 2472–2482.
[58] (a) Y. Fu, D. Sun, Y. Chen, R. Huang, Z. Ding, X. Fu, Z. Li, Angew. Chem., Int. Ed. 51 (2012) 3364–3367;
(b) D. Sun, Y. Fu, W. Liu, L. Ye, D. Wang, L. Yang, X. Fu, Z. Li, Chem. Eur. J. 19 (2013) 14279–14285.
[59] D. Chen, H. Xing, C. Wang, Z. Su, J. Mater. Chem. A 4 (2016) 2657–2662.
[60] (a) I.A. Cohen, B.C. Chow, Inorg. Chem. 13 (1974) 488–489;
(b) B.B. Wayland, A. Duttaahmed, B.A. Woods, J. Chem. Soc. Chem. Commun. (1983) 142–143;
(c) B.B. Wayland, A.E. Sherry, G. Poszmik, A.G. Bunn, J. Am. Chem. Soc. 114 (1992) 1673–1681;
(d) J.P. Collman, R. Boulatov, Inorg. Chem. 40 (2010) 560–563;
(e) S. Yamazaki, M. Yao, M. Asahi, H. Sato, A. Yamano, T. Ioroi, Dalton Trans. 44 (2015) 13823–13827.
[61] A.J. Howarth, A.W. Peters, N.A. Vermeulen, T.C. Wang, J.T. Hupp, O.K. Farha, Chem. Mater. 29 (2017) 26–39.
[62] S. Hamad, N.C. Hernandez, A.G. Aziz, A.R. Ruiz-Salvador, S. Calero, R. Grau-Crespo, J. Mater. Chem. A. 3 (2015) 23458–23465.